Vision-based Collision Avoidance for Personal Aerial Vehicles using Dynamic Potential Fields

Faizan Rehmatullah
Institute for Aerospace Studies
University of Toronto
Toronto, Canada
Email: faizan.rehmatullah@mail.utoronto.ca

Jonathan Kelly
Institute for Aerospace Studies
University of Toronto
Toronto, Canada
Email: jkelly@utias.utoronto.ca

***Abstract*—In this paper we present a prototype system that aids the operator of a Personal Air Vehicle (PAV) by actively monitoring vehicle surroundings and providing autonomous control inputs for obstacle avoidance. The prototype is developed for a Personal Air Transportation System (PATS) that will enable human operators with low level of technical knowledge to use aerial vehicles for a day-to-day commute. While most collision avoidance systems used on human controlled vehicles override operator input, our proposed system allows the operator to be in control of the vehicle at all times. Our approach uses a dynamic potential field to generate pseudo repulsive forces that, when converted into control inputs, force the vehicle on a trajectory around the obstacle. By allowing the vehicle control input to be the sum of operator controls and collision avoidance controls, the system ensures that the operator is in control of the vehicle at all times. We first present a dynamic repulsive potential function and then provide a generic control architecture required to implement the collision avoidance system on a mobile platform. Further, extensive computer simulations of the proposed algorithm are performed on a quadcopter model, followed by hardware experiments on a stereo vision sensor. The proposed collision avoidance system is computationally inexpensive and can be used with any sensor that can produce a point cloud for obstacle detection.**

***Keywords*-collision avoidance; potential fields; personal aerial vehicles; stereo vision; mobile robots**

I. Introduction

Road traffic congestion is a growing concern for all major cities in the world [1]. While there has been a continuous increase in the number of vehicles, limited expansion of the road infrastructure has pushed the system to its saturation point. According to the Federation of Canadian Municipalities, city traffic costs 32 days worth of productive work time annually, adding up to losses of around $10 billion for the Canadian economy [2]. To address this issue, active research is being done in the area of Intelligent Transportation Systems (ITS) and self-driving cars. While substantial improvements in traffic congestion are expected from these systems, the solutions are temporary as they will not be able to cope up with the increasing demand for personal mobility. The development of a Personal Air Transportation System (PATS) is a promising solution to this problem.

A vast amount of research has been done on the development of a Personal Air Vehicle (PAV) [3], [4], [5], however the research on Personal Air Transportation Systems (PATS) has been very limited. The current aerial transportation system depends on Air Traffic Controllers (ATC) for navigation and skilled pilots for aircraft control. In contrast, a successful PATS will enable human operators with a low level of technical knowledge to control a vehicle without any navigational directions from an ATC [1], [6]. Similar to roadways, PATS will have predefined three-dimensional airways used for navigation. As a PAV is expected to be controlled by people with limited technical knowledge, it is critical to develop a fail-safe navigation and collision avoidance system. If the collision avoidance problem is not addressed, the catastrophic results of aerial collisions will limit the use of PAVs in civil airspace [7].

The focus of this research is to develop a collision avoidance system for PATS. In this research, a stereo vision sensor is used to provide a point cloud representation of the world [8], [9], [10], while a Virtual Potential Field (VPF) is used for collision avoidance [11], [12]. A VPF utilizes potential field theory to calculate a virtual repulsive force that is used to direct the vehicle away from the identified obstacle. The virtual force vector is mapped onto vehicle control inputs to provide the desired collision avoidance trajectory. The framework developed in this research is universal as it can be implemented on a variety of mobile platforms including Micro Air Vehicles (MAVs), Unmanned Aerial Vehicles (UAVs), self-driving cars, and rovers.

II. Related Work

A. Personal Air Transportation System

Extensive work on PATS has been done under a European commission funded project called *myCopter* [1]. The project, which started in 2011 and ended in 2014, was aimed at providing a concept of operations for PATS infrastructure. A similar study was conducted by the National Aeronautics and Space Administration (NASA) in 2006 [6]. The study highlighted how the existing Federal Aviation Administration (FAA) aerial transportation infrastructure is incapable

of handling the air traffic volume generated by PATS. The study from [6] identifies the key requirements for a PAV and the PATS infrastructure. Among the identified requirements for PATS, active collision avoidance on a human controlled PAV is the most critical.

B. Collision Avoidance

1) Optic Flow Based Collision Avoidance: Optic flow is a predominant collision avoidance technique used with monocular camera systems. The principle of optic flow makes use of motion parallax to determine the flow vector field. The Lucas-Kanade algorithm, which uses intensity gradients to estimate the flow vectors, was employed by Gosiewski and Cieśluk in [13]. Robust optic flow computation techniques were developed by Alireza and Suter in [14] and Beauchemin and Barron in [15]. A Lukas-Kanade gradient based optic flow method was also used by Zufferey and Beyeler in [16]. In the paper, the authors developed a control strategy based on a series of optic flow detectors pointing in different viewing directions around an aircraft. The resulting optic flow vector field was mapped onto control inputs for collision avoidance.

Optic flow techniques work well with a single obstacle and for flights in canyon-style streets. The flow method has difficulty dealing with large numbers of obstacles that have uniform texture such as, for example, tall buildings of a similar colour. This issue eliminates the possibility of using optic flow as means of performing collision avoidance for PAVs in the PATS infrastructure.

2) Potential Field Based Collision Avoidance: An approach for path planning using potential functions was first introduced by Khatib [17]. Chuang and Ahuja [18] extended the idea from a point-based potential function to one that involving structured obstacle geometries. The concept was then extended further to multiagent systems by Dimarogonas [19]. Other applications of potential fields include [12], [20], [21].

An extension to the concept of static potential fields was made by Ge and Cui [22], [23]. They introduced a dynamic potential function which varies with the relative velocity between the vehicle and obstacle. Potential functions presented in [22] and [23] form the basis for the collision avoidance strategy proposed in this research.

III. Dynamic Potential and Force Fields

The proposed collision avoidance algorithm uses an artificial Repulsive Potential Field (RPF) to determine control inputs required for obstacle avoidance. Potential fields provide a promising solution to the collision avoidance problem for PAVs. The basic concept is to fill the space around a vehicle with an artificial repulsive potential field. A Repulsive Potential Field (RPF) centered on the vehicle establishes a safety zone; the presence of an obstacle inside this safety zone activates the collision avoidance controller. The magnitude and direction of force generated by the repulsive potential is mapped onto control inputs in order to drive the vehicle away from the detected obstacle. The repulsive potential field used in this research is adopted from [22] and [23].

A. Assumptions

Following assumptions were made while developing a RPF for dynamic systems:

1) The vehicle is equipped with a sensor that can detect an obstacle as a point or clouds of points.
2) Obstacles are defined by a set of points $U = \{u_1, u_2, u_3 ... u_n\}$ within a Sphere of Influence (SOI).
3) The relative positions and velocities between the vehicle and all points in the set U can be determined.

B. Sphere of Influence

A SOI is defined by the horizontal angle θ_h and the vertical angle ψ_v of the Field of View (FOV) of the vision sensor(s). The radius of the SOI, given by r_{soi} defines the boundary between activation and deactivation of the collision avoidance system. A critical radius r_m, which is the distance traveled by the vehicle under maximum deceleration, specifies the distance at which the repulsive potential goes to infinity.

The defined sphere of influence provides a safety zone in which the collision avoidance system is active. The sphere of influence is shown graphically in Figure 1.

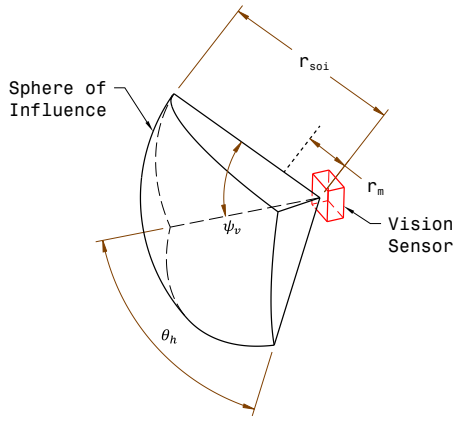

Figure 1. The SOI is defined by the horizontal angle θ_h and vertical angle ψ_v of the FOV of the vision sensor. The radius of sphere of influence r_{soi} is defined by the characteristics of the vehicle.

C. Single Point Repulsive Potential Field

The proposed repulsive potential field is analogous to the electric potential field. The magnitude is inversely proportional to the distance between the vehicle and the obstacle and is also dependent on the relative velocity between them. By Assumption 3, the relative velocity between the vehicle

and any point u in the set U can be determined and is given by

$$v_{vo}(t) = [\vec{\mathbf{v_v}}(t) - \vec{\mathbf{v_o}}(t)]^\intercal \vec{\mathbf{n_{vo}}} \tag{1}$$

where $\vec{\mathbf{n_{vo}}}$ is a unit vector pointing from vehicle to the obstacle, $\vec{\mathbf{v_v}}$ is the velocity of the vehicle and $\vec{\mathbf{v_o}}$ is the velocity of the obstacle.

To include the effect of vehicle limitations into the repulsive potential function, the distance traveled by the vehicle under maximum deceleration is defined by

$$r_m = \frac{v_{vo}^2}{2a_{max}} \tag{2}$$

where r_m is the distance traveled and a_{max} is the maximum deceleration that can be achieved.

If r_{soi} is the radius of the sphere of influence, r_m is the distance traveled by the vehicle under maximum declaration, and r is the shortest distance between the vehicle and a point u, then the function defining the repulsive potential for a single point in the set U is given by

$$U_{rep}\left(\vec{\mathbf{p}}, \vec{\mathbf{v}}\right) = \begin{cases} 0, & \text{if } r - r_m \geq r_{soi} \text{ or } v_{vo} \leq 0 \\ \mu\left(\dfrac{1}{r(\vec{\mathbf{p_v}}, \vec{\mathbf{p_o}}) - r_m} - \dfrac{1}{r_{soi}}\right), & \\ & \text{if } 0 < r - r_m < r_{soi} \text{ and } v_{vo} > 0 \\ \infty, & \text{if } r < r_m \text{ and } v_{vo} > 0 \end{cases} \tag{3}$$

where μ is the constant of proportionality, $\vec{\mathbf{p_o}}$ is the vector defining the position of the obstacle and $\vec{\mathbf{p_v}}$ is the vector defining the position of the vehicle.

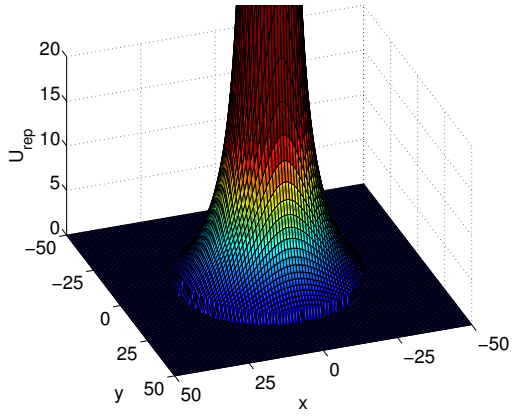

Figure 2. Plot of the potential function defined in Equation 3. The potential function is undefined for $r < r_m$ and goes to 0 for r - $r_m \geq r_{soi}$. The following parameters are used to define the potential function; r_{soi} = 30, r_m = 5, μ = 200.

The potential function defined in Equation 3 is plotted in Figure 2. The magnitude of the potential goes to 0 at r_{soi} and approaches ∞ as the distance between the vehicle and the obstacle approaches r_m. Between r_{soi} and r_m the repulsive potential is inversely proportional to the distance between the vehicle and the obstacle.

Equation 3 assumes that obstacles can be detected over the entire 360° range around the vehicle. It is known that due to a limited sensor FOV, the vehicle can only detect obstacles within the SOI limited by the FOV. A modified repulsive potential function U_{rep_a} that incorporates detection limitations is defined by

$$U_{rep_a}\left(\vec{\mathbf{p}}, \vec{\mathbf{v}}\right) = \begin{cases} U_{rep}, & \text{if } \left(-\dfrac{\theta_h}{2} \leq \theta \leq \dfrac{\theta_h}{2}\right) \text{ or } \left(-\dfrac{\psi_v}{2} \leq \psi \leq \dfrac{\psi_v}{2}\right) \\ 0, & \text{otherwise} \end{cases} \tag{4}$$

where θ is the polar angle and ψ is the azimuthal angle.

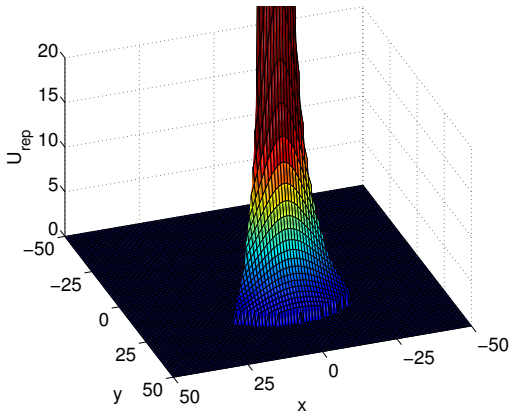

Figure 3. Plot of the modified potential function defined in Equation 4. The potential function is undefined for $r < r_m$ and goes to 0 for r - $r_m \geq r_{soi}$. The potential function is limited by the SOI. Following parameters are used to define the potential function; r_{soi} = 30, r_m = 5, μ = 200, θ_h = 98°. Since the potential function is plotted on a 2-D meshgrid ψ_v is not included.

The potential function defined in Equation 4 is plotted in Figure 3. The potential function is similar to the one defined in Equation 3 and Figure 2 but is bounded by the FOV of the sensor.

D. Single Point Repulsive Force Field

While the repulsive potential field defines the energy of the system, a repulsive force field is required to determine the direction that the vehicle should follow to avoid an obstacle. When the obstacle is inside the sphere of influence, a force vector is generated which is defined by the negative of the gradient of the potential function given in Equation 3 and Equation 4.

Vectors defining the repulsive force field provide the magnitude/intensity of the signal for avoidance control maneuvers, while the direction of the force vector defines the direction that the vehicle should follow to avoid obstacles.

The repulsive force field is given by

$$\begin{aligned} F_{rep}(\vec{\mathbf{p}}, \vec{\mathbf{v}}) &= -\nabla U_{rep}(\vec{\mathbf{p}}, \vec{\mathbf{v}}) \\ &= -\nabla_p U_{rep}(\vec{\mathbf{p}}, \vec{\mathbf{v}}) - \nabla_v U_{rep}(\vec{\mathbf{p}}, \vec{\mathbf{v}}) \end{aligned} \tag{5}$$

where $\vec{\mathbf{p}}$ is the position vector and $\vec{\mathbf{v}}$ is the velocity vector.

The magnitude of velocity between the vehicle and the obstacle is given by

$$v_{vo}(t) = [\vec{\mathbf{v_v}}(t) - \vec{\mathbf{v_o}}(t)]^\intercal \vec{\mathbf{n_{vo}}} \tag{6}$$

where $\vec{\mathbf{n_{vo}}}$ is defined by

$$\vec{\mathbf{n_{vo}}} = \frac{\vec{\mathbf{p_o}}(t) - \vec{\mathbf{p_v}}(t)}{\|\vec{\mathbf{p_o}}(t) - \vec{\mathbf{p_v}}(t)\|}, \tag{7}$$

that is, $\vec{\mathbf{n_{vo}}}$ is the vector pointing from the vehicle to the obstacle which provides the direction of the obstacle in the body frame.

The gradient of $v_{vo}(t)$ with respect to $\vec{\mathbf{v}}$ is given by

$$\nabla_v v_{vo}(t) = \vec{\mathbf{n_{vo}}} \tag{8}$$

and that with respect to $\vec{\mathbf{p}}$ is given by

$$\nabla_p v_{vo}(t) = -\frac{1}{\|\vec{\mathbf{p_o}}(t) - \vec{\mathbf{p_v}}(t)\|}[v_{vo}(t)\vec{\mathbf{n_{vo}}} - (\vec{\mathbf{v_v}}(t) - \vec{\mathbf{v_o}}(t))] \tag{9}$$

Taking r_m from Equation 2, substituting it in Equation 3 and calculating the gradient of the potential function, we get the following force field

$$\vec{\mathbf{F_{rep}}}(\vec{\mathbf{p}}, \vec{\mathbf{v}}) = \begin{cases} 0, & \text{if } r - r_m \geq r_{soi} \text{ or } v_{vo} \leq 0 \\ \vec{\mathbf{F_{rep_1}}} + \vec{\mathbf{F_{rep_2}}}, & \\ & \text{if } 0 < r - r_m < r_{soi} \text{ and } v_{vo} > 0 \\ \infty, & \text{if } r < r_m \text{ and } v_{vo} > 0 \end{cases} \tag{10}$$

where

$$\vec{\mathbf{F_{rep_1}}} = \frac{-\mu}{(r(\vec{\mathbf{p_v}}, \vec{\mathbf{p_o}}) - r_m)^2}\left(1 + \frac{v_{vo}}{a_{max}}\right)\vec{\mathbf{n_{vo}}} \tag{11}$$

$$\vec{\mathbf{F_{rep_2}}} = \frac{\mu v_{vo}(\vec{\mathbf{v_v}}(t) - \vec{\mathbf{v_o}}(t) - v_{vo}(t)\vec{\mathbf{n_{vo}}})}{r(\vec{\mathbf{p_v}}, \vec{\mathbf{p_o}}) a_{max}(r(\vec{\mathbf{p_v}}, \vec{\mathbf{p_o}}) - r_m)^2} \tag{12}$$

The repulsive force field in Equation 10, Equation 11 and Equation 12 is defined using a unit vector $\vec{\mathbf{n_{vo}}}$ pointing from the vehicle to the obstacle. Components of $\vec{\mathbf{n_{vo}}}$ resolve the force vector into its components in the body frame.

E. Repulsive Force Field from a Point Cloud

The repulsive potential and force field due to a single point can be extended to a point cloud. If the point cloud generated around the object is defined by points in the set U, then the force exerted by every point in U can be added to determine the maneuver direction. An average force is calculated to determine the maneuver magnitude. The equation for normalized total force is give by

$$\hat{\mathbf{F}}_{\mathbf{rep_{tot}}} = \frac{\sum_{i=1}^{n} \vec{\mathbf{F_{rep}}}_i}{n} \tag{13}$$

where n is the total number of detected points, i.e., all points in the set U. As the point cloud enters the sphere of influence, the vehicle responds to force $\hat{\mathbf{F}}_{\mathbf{rep_{tot}}}$ specified in Equation 13.

IV. Control Architecture

When used on a PAV, the collision avoidance system will work in conjunction with the primary Guidance, Navigation and Control (GNC) system (which may include a human controller) while actively monitoring the presence of obstacles in its surroundings. A generic control architecture for the proposed Collision Avoidance System (CAS) is shown in Figure 4.

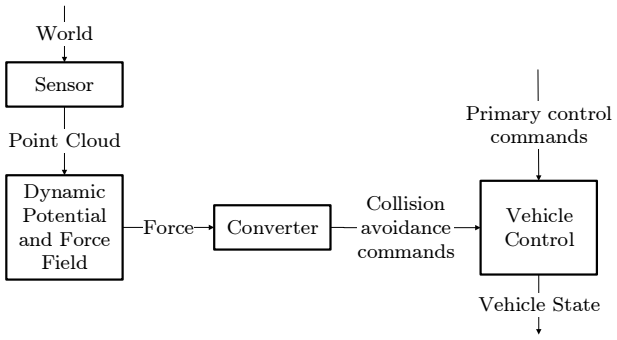

Figure 4. Generic control architecture for the proposed collision avoidance system.

The following four blocks are required for implementation of the collision avoidance system:

1) Sensor
2) Dynamic Potential and Force Field (DPFF)
3) Converter
4) Vehicle Control

A. Sensor

The sensor provides a 3 Dimensional (3D) point cloud which is used to calculate the distance to a detected obstacle.

B. Dynamic Potential and Force Field

The dynamic potential and force field block uses the point cloud generated from the sensor and determines the relative distance and velocity between the vehicle and obstacle. This information is then used to calculate the virtual repulsive force using equations provided in Section III.

C. Converter

The converter block translates repulsive forces from the dynamic potential and force field block into control inputs. The calculated forces are first capped at the maximum allowable force F_{max}. The saturated force is then converted into control inputs using gains defined by

$$K = \frac{\theta_{max}}{F_{max}} \tag{14}$$

where θ_{max} is the maximum value of the control variable[1] and F_{max} represents the force at which the vehicle applies maximum control input.

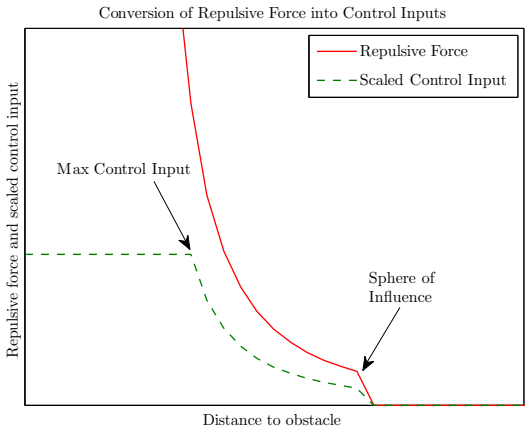

Figure 5. Mapping between calculated repulsive force and control input. Maximum control input corresponds to the value that saturates the actuator. While the force can go to infinity, control input is capped at the saturation point. The control input curve follows a trend similar to that of the calculated repulsive force.

Values for θ_{max} and F_{max} are platform dependent. These parameters can be tuned to achieve the desired vehicle response. Figure 5 shows the relationship between the repulsive force and the mapped control inputs.

D. Vehicle Control

The vehicle control block accepts inputs from the global navigation system through primary control commands as well as collision avoidance inputs from the converter block. Global navigation can either be through a human controlled system (where a pilot provides navigation inputs) or it can be autonomous. The vehicle control loop block actively accepts command inputs from both streams and provides the vehicle controller with the sum of the two. When an obstacle is outside the sphere of influence, commands from the collision avoidance system are 0. Once an obstacle is detected inside the sphere of influence, collision avoidance commands are added to the primary navigation commands to enable the vehicle to avoid the obstacle.

V. Simulation

This section presents a Simulink model developed to simulate the collision avoidance system. A cube shaped obstacle with 500 randomly distributed points is generated while the entire control architecture for the collision avoidance system discussed in Section IV is modeled on a quadcopter Unmanned Aerial Vehicle (UAV). An open source quadcopter dynamics controller is used to simulate vehicle dynamics. The simulation reference frame is shown in Figure 6.

[1]Since we simulate this system on a quadcopter UAV, the maximum control input in the z direction is the maximum available thrust while the maximum control input in the x and y directions corresponds to the maximum allowable roll and pitch angles, respectively.

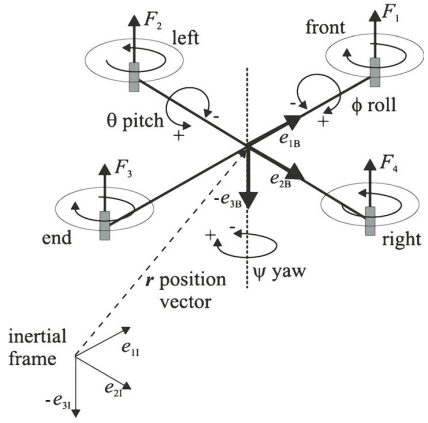

Figure 6. Quadcopter reference frame used for simulation [24]

A. Simulation Parameters

The following values are used for the various parameter of the system:

1) A maximum deceleration (a_{max}) of $5m/s^2$ is chosen for this simulation. This corresponds to a maximum lateral g-force of $0.5g$.
2) The radius of sphere of influence (r_{soi}) is set to $5m$.
3) The constant of proportionality (μ) is set to 20. This corresponds to an increase or decrease in the magnitude of the potential field which corresponds to aggressiveness in the vehicle response.
4) The maximum force in the x, y, and z directions is set at 10. A higher maximum force at the same maximum control input would correspond to a lower gain and will thus lead to less aggressive maneuvers and closer approach distance.
5) The maximum roll and pitch angles for the vehicle are set at 45° while the maximum thrust is set at 500.
6) The mass of the quadcopter is 4 kg.
7) The radius of the quadcopter is $0.165m$.
8) The moment of inertia $\mathbf{I}$ matrix of the quadcopter is given by

$$\mathbf{I} = \begin{bmatrix} 0.082 & 0 & 0 \\ 0 & 0.082 & 0 \\ 0 & 0 & 0.1490 \end{bmatrix} \quad (15)$$

B. Simulation Results and Discussion

The system was tested for various different approach cases. In each simulation run, the location of the robot, the repulsive forces, the control inputs, and the minimum separation distance were recorded. Results are presented for a head-on constant velocity approach in $+x$ direction. The

vehicle trajectory is shown in Figure 7, the repulsive forces are shown in Figure 8, and the control inputs are shown in Figure 9

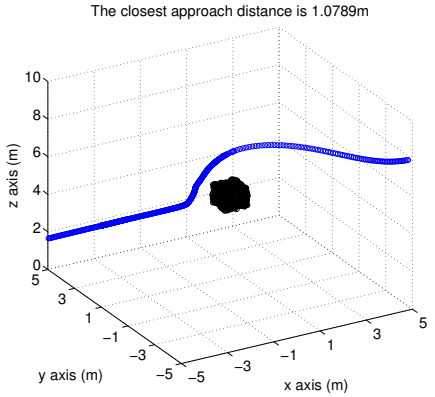

Figure 7. Vehicle trajectory for head-on approach in $+x$ direction.

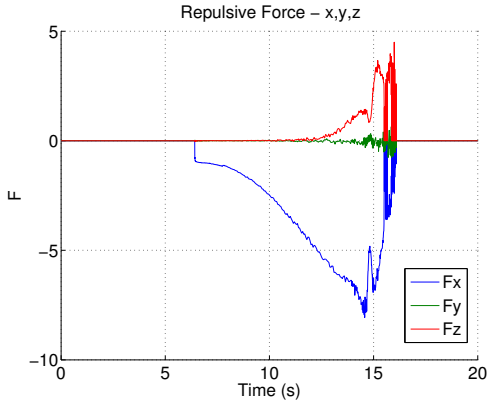

Figure 8. Repulsive forces in x, y, and z directions during collision avoidance.

As observed in Figure 7, the quadcopter starts moving towards the obstacle (head-on) at a constant velocity. It slows down once the obstacle enters the sphere of influence and then stops at a distance of $1.07m$. At that point, asymmetry in the vertical direction caused by the uneven distribution of points together with asymmetry in the quadcopter thrust response allows the vehicle to rise above the obstacle.

The control response curves shown in Figure 9 provide a picture of the control inputs seen by the vehicle during the collision avoidance maneuver. Figure 8 shows the forces in the x, y, and z directions. As observed, the force in the x direction is 0 initially and then sharply increases at a distance of $5m$ from the obstacle, i.e., the location where the vehicle's sphere of influence begins. Repulsive force in x direction pitches the quadcopter up, slowing its velocity. At this point, forces accumulate in the z direction leading to an increase in vehicle thrust. The vehicle regains forward velocity once it has climbed over the obstacle. When safely

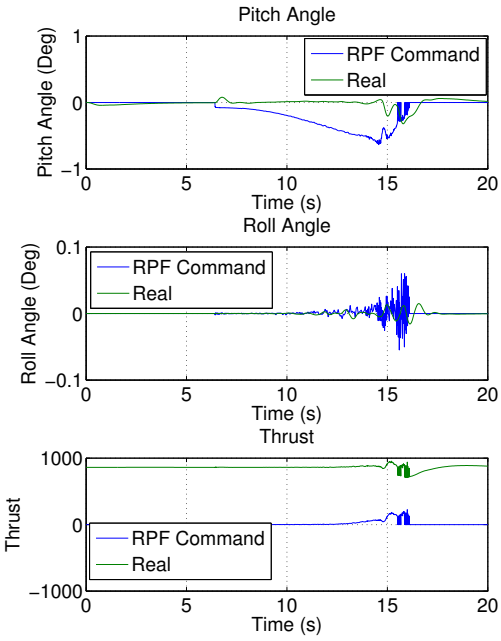

Figure 9. Roll, pitch, and thrust control inputs during collision avoidance.

past the obstacle, the vehicle starts to catch up with the x-direction command input and no force and hence no collision avoidance control input is observed. During this maneuver, minor roll oscillations are seen. These are small enough to have no significant impact on the vehicle motion.

VI. Experimentation

To test the effectiveness of the proposed collision avoidance system, indoor experiments were performed with a VI-Sensor stereo visual-inertial sensor from Skybotix [25]. The experiments involved a human test subject approaching the sensor from different directions. The collision avoidance system was implemented using the Robot Operating System (ROS). Our experimental setup is shown in Figure 10. The left and right camera image streams from the VI-Sensor were initially passed through an open source block-matching stereo pipeline to generate a 3D point cloud. The resulting cloud was then down sampled using a voxel grid filter before being passed to the collision avoidance algorithm.

A. System Parameters

The following values were used for the various system parameters:

1) A maximum deceleration (a_{max}) of $5m/s^2$.
2) A sphere of influence radius (r_{soi}) of $2.5m$.
3) A constant of proportionality (μ) of 20.
4) Maximum force in the x, y, and z directions of 10.
5) Maximum roll, pitch, and thrust values for the vehicle of 1.

To ensure that the vehicle was not affected by sensor noise, a lower bound for collision avoidance control input was set at 0.1. Point clouds and resulting forces and control inputs are presented in the optical frame of the left camera (X Right, Y Down, Z out). In these experiments the relative velocity between the vehicle and obstacle was not included, thus the potential function and the force field values depended on the distance only.

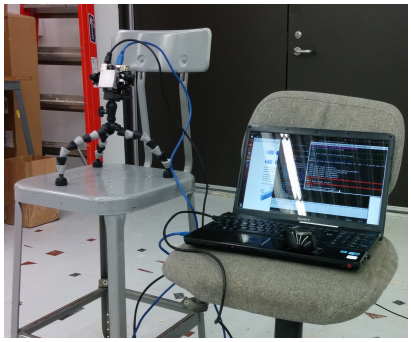

Figure 10. Experimental Setup for the collision avoidance system. The VI-Sensor is kept stationary on a tripod. A gigabit Ethernet cable is used for communication to the laptop computer while the sensor is powered through a USB port

B. Forward-Backward Maneuver

A forward-backward approach towards an obstacle is the most critical case for a collision avoidance system. While the sensor was fixed on a stationary platform, a human test subject walked towards the sensor. As observed in Figure 11, repulsive forces and control inputs were generated once the (human) obstacle entered the sphere of influence. In the forward-backward case, the majority of control input is in the -z direction. If mounted on a quadcopter UAV, this would result in a pitch up maneuver, slowing the vehicle down. Due to an asymmetric point cloud distribution, a small amount of roll and pitch control input is also calculated.

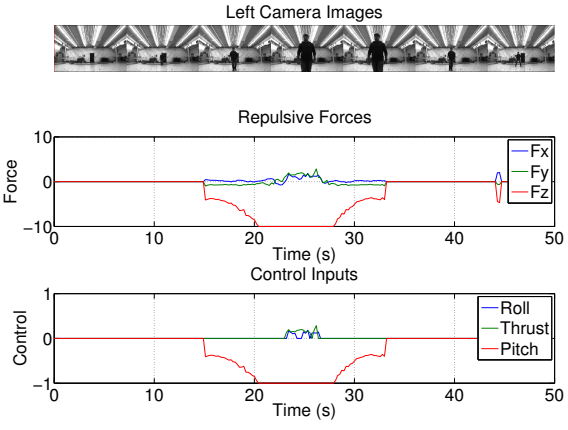

Figure 11. Repulsive forces and control inputs during a forward-backward maneuver. Control inputs less than 0.1 are filtered. It can be seen that a major part of the control input comes from the force in the -z direction.

C. Left-Right Maneuver

In the case of a left-right maneuver, the thrust input remains at 0 since the point cloud is vertically symmetric. As observed in Figure 12, once an obstacle enters the sphere of influence from the left, positive roll and a positive pitch values are calculated. When mapped onto the vehicle control inputs, this pushes the vehicle away from the obstacle. Similar control inputs are observed when an object approaches the sphere of influence from the right.

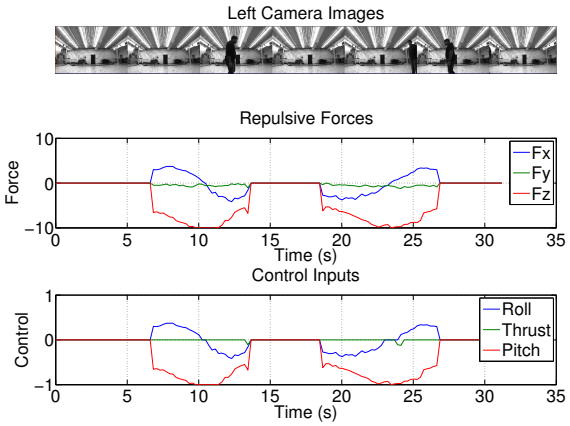

Figure 12. Repulsive forces and control inputs during a left-right maneuver in front of the sensor.

D. Up-Down Maneuver

In case of an up-down maneuver, the pitch input remains constant while the roll input is approximately 0 throughout. A roll input is calculated when the test subject enters and exits the sphere of influence (from the left). When the obstacle in under the camera, a force in the negative y direction is observed; this will push the vehicle up, away from the obstacle.

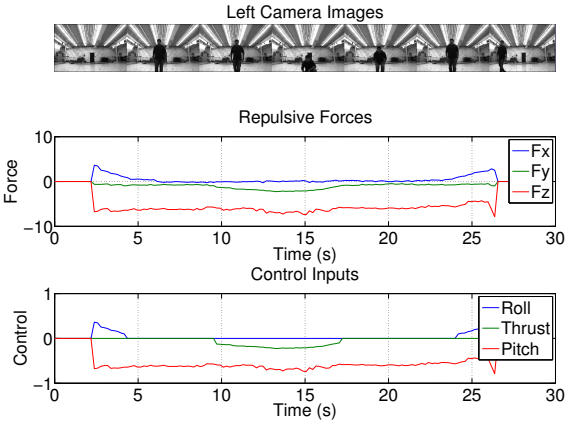

Figure 13. Repulsive forces and control inputs during a up-down maneuver in front of the sensor.

VII. Conclusion and Future Work

In this paper a potential field-based collision avoidance system was presented for personal aerial vehicles. A dynamic potential field was used to repel the vehicle away from an obstacle. On a human-controlled PAV, the resulting repulsive control forces would not only move the vehicle away from the obstacle but would also provide inputs to a haptic feedback system.

The collision avoidance implementation is computationally inexpensive and can be used with any sensor that can provide a point or a cloud of points for obstacle detection. It can potentially be implemented for indoor and outdoor environments and can be used with primary navigation systems on a Micro Aerial Vehicle (MAV), an UAV, or a rover. Further experiments are being conducted to asses the effectiveness of the system with a range of sensor and vehicle platforms.

Extensive human-factors research on the system implemented with haptic feedback control would further validate the effectiveness of the proposed collision avoidance system. Tests in outdoor environments at higher altitude would expose the algorithm to harsher condition. On a real PAV, a multi-sensor system, using probabilistic estimates of the point cloud, could be implemented to further improve the robustness of the proposed algorithm.

References

[1] M. Jump, G. D. Padfield, and M. D. White, "myCopter: Enabling Technologies for Personal Air Transport Systems," in *The Future Rotorcraft: Enabling Capability through the Application of Technology*, Royal Aeronautical Society, 2011.

[2] "Commuting in Canada: How Your Drive To Work Stacks Up." http://www.insurancehotline.com, 2015. [Online; accessed 21-Jan-2015].

[3] "Aerocar." http://www.aerocar.com/, 2015. [Online; accessed 12-Feb-2015].

[4] "Terrafugica." http://www.terrafugia.com/, 2015. [Online; accessed 12-Feb-2015].

[5] "Carplane." http://www.carplane.com/, 2015. [Online; accessed 12-Feb-2015].

[6] "NASA Personal Air Transportation Technologies." http://www.sae.org/technical/papers/2006-01-2413, 2006. [Online; accessed 12-Feb-2015].

[7] M. T. Degarmo and M. T. Degarmo, "Issues Concerning Integration of Unmanned Aerial Vehicles in Civil Airspace Issues Concerning Integration of Unmanned Aerial Vehicles in Civil Airspace," no. November, 2004.

[8] L. Mejias, J. McNamara, Scott andq Lai, and J. Ford, "Vision-based detection and tracking of aerial targets for UAV collision avoidance," in *IEEE/RSJ 2010 International Conference on Intelligent Robots and Systems, IROS 2010 - Conference Proceedings*, pp. 87–92, 2010.

[9] H. Alvarez, L. M. Paz, J. Sturm, and D. Cremers, "Collision Avoidance for Quadrotors with a Monocular Camera," pp. 1–14.

[10] L. Mejias, S. McNamara, J. Lai, and J. Ford, "Vision-based detection and tracking of aerial targets for UAV collision avoidance," in *IEEE/RSJ 2010 International Conference on Intelligent Robots and Systems, IROS 2010 - Conference Proceedings*, pp. 87–92, 2010.

[11] Bornenstein, Johan, Yorem, and Koren, "Real-Time Obstacle Avoidance for Fast Mobile Robots," vol. 19, no. 5, pp. 1179–1187, 1989.

[12] Reston and Virigina, "UAV Trajectory Design Using Total Field Collision Avoidance," pp. 1–11, August 2003.

[13] Gosiewski, Zdzislaw and Ciesluk, Jakub and Ambroziak, Leszek, "Vision-based obstacle avoidance for unmanned aerial vehicles," in *2011 4th International Congress on Image and Signal Processing*, vol. 4, pp. 2020–2025, 2011.

[14] Alireza BAB-Hadiashar and David Suter, "Robust optic flow computation," *International Journal of Computer Vision*, vol. 29, 1998.

[15] Beauchemin S. S. and Barron J. L., "The computation of optic flow," *ACM Computing Surveys*, vol. 27, 1995.

[16] Jean-Christophe Zufferey and Antoine Beyeler and Dario Floreano, "Autonomous flight at low altitude with vision-based collision avoidance and GPS-based path following," in *2010 IEEE International Conference on Robotics and Automation*, (Anchorage, Alaska, USA), pp. 3329–3334, May 2010.

[17] Khatib, "Commande dynamique dans I'espace opkrational des robots manipulateurs en prCsence d'obstacles," *Ph.D. dissertation, Ecole na- tionale Supkieure de I'AeCronatique et de I'Espace (ENSAE), France*, 1980.

[18] Jen-Hui Chuang and Narendra Ahuja Abstract—An, "An Analytically Tractable Potential Field Model of Free Space and its Application in Obstacle Avoidance," *IEEE Transactions on Systems, Man and Cybernetics*, vol. 28, pp. 729–736, Oct. 1998.

[19] Dimos V. Dimarogonas, "Sufficient Conditions for Decentralized Potential Functions Based Controllers Using Canonical Vector Fields," *IEEE Transactions on Automatic Control*, vol. 57, pp. 2621–2626, Oct. 2012.

[20] J. Bornenstein and K. Yorem, "Real-Time Obstacle Avoidance for Fast Mobile Robots," vol. 19, no. 5, pp. 1179–1187, 1989.

[21] Elon Rimon, and Daniel E. Koditschek, "Exact Robot Navigation Using Artificial Potential Functions," *IEEE Transactions on Robotics and Automation*, vol. 8, pp. 501–518, Oct. 2992.

[22] S. Ge and Y. Cui, "New potential functions for mobile robot path planning," *IEEE Transactions on Robotics and Automation*, vol. 16, no. 5, pp. 615–620, 2000.

[23] G. S.S., Cui, and Y.J., "Dynamic motion planning for mobile robots using potential field method," *Autonomous Robots*, pp. 207–222, 2002.

[24] H. Bolandia, M. Rezaei, and R. Mohsenipour, "Attitude control of a quadrotor with optimized pid controller," vol. 4, pp. 335–342, 2013.

[25] "VI-Sensor — Skybotix AG.." http://www.skybotix.com/, 2014. [Online; accessed 24-Jan-2015].